

Manipulation of topology by electric field in breathing kagome lattice

Yu Xie,¹ Ke Ji,² Jun He,¹ Xiaofan Shen,³ Dinghui Wang,¹ and Junting Zhang^{1,*}

¹*School of Materials Science and Physics, China University of Mining and Technology, Xuzhou 221116, China*

²*Department of Physics, University of Antwerp, Groenenborgerlaan 171, B-2020 Antwerp, Belgium*

³*National Laboratory of Solid State Microstructures and Physics School, Nanjing University, Nanjing 210093, China*

Magnetic kagome lattices have attracted much attention recently due to the interplay of band topology with magnetism and electronic correlations, which give rise to a variety of exotic quantum states. A common structural distortion of the kagome lattice is the breathing mode, which can significantly influence the magnetism and band characteristics. However, the modulation of breathing mode and the associated topological phenomena remain rarely explored. Here, we demonstrate that the coupling of breathing modes with ferroelectricity, magnetism, and band topology in the M_3X_8 monolayer system enables electric field manipulation of topological spin structure and electronic states. The breathing mode mainly occurs in materials containing early $4d/5d$ transition metal elements and can be reversed or even suppressed via ferroelectric switching in low-barrier materials. Importantly, electric field-induced switching of the breathing mode can alter the chirality of the topological spin structure, or trigger a transition from a topological trivial insulator to a Chern insulator. This work paves the way for exploring novel physical phenomena driven by breathing modes in kagome materials.

The interplay of nontrivial topology, magnetism, and electron correlations in kagome lattice leads to diverse emerging phenomena and novel quantum states, such as unconventional superconductivity, charge and spin density waves, quantum spin liquids, topological states, and flat bands¹⁻⁶. For instance, AV_3Sb_5 ($A = K, Rb, Cs$), a representative class of kagome materials, has attracted significant attention for exhibiting superconductivity, charge and pair density waves, nematic phase, Dirac semimetal, and large anomalous Hall effect in a single material⁷⁻¹⁴. The combination of intrinsic magnetism and topology in kagome magnets causes a variety of topological electronic states, enabling topological quantum phenomena such as the quantum anomalous Hall effect and fractional quantum Hall effect¹⁵⁻¹⁸. In addition, real space topological spin textures, magnetic skyrmions, have been identified in some frustrated kagome magnets¹⁹⁻²¹.

A common structural distortion in the kagome lattice is the breathing mode⁶, which can not only modulate electron correlation, magnetic coupling and band topology, but also break the spatial inversion symmetry²¹⁻²⁴. Therefore, the breathing kagome lattice also provides a good platform for exploring physical effects related to inversion symmetry breaking, such as spin polarization, valley-contrast physics, and magnetoelectric multiferroics²⁵⁻²⁹. Nb_3X_8 ($X = Cl, Br, I$), a representative material family with a breathing kagome lattice, has gained attention as an emerging class of kagome materials for its exotic correlated electronic behaviors, such as topological flat bands³⁰⁻³², Mott-insulating state^{33, 34}, and quantum spin liquid state^{35, 36}. Due to their weak van der Waals coupling, layered Nb_3X_8 crystals can be easily exfoliated into monolayers²⁴, making them an ideal system for studying novel physical effects driven by breathing mode in two-dimensional (2D) kagome lattice.

Breathing mode may provide an additional degree of freedom to manipulate the exotic electronic states and magnetism of kagome materials. However, its control via external fields, particularly electric field, has not yet been demonstrated. In this work, we first screened 2D kagome materials with breathing mode in the M_3X_8 (M is a transition metal ion and X is a halide ion) monolayer system, which mainly exist in compounds containing early $4d$ or $5d$ ions. We then demonstrate that in some low-barrier materials, an out-of-plane pulsed electric field can reverse the breathing mode or even suppress it through a ferroelectric-to-paraelectric phase transition. Altering the sign or amplitude of the breathing mode with an electric field enables the chirality of topological spin textures to be switched or induces a topological phase transition, respectively.

Results

Screening of materials with breathing mode. The M_3X_8 monolayer consists of edge-sharing octahedra, in which the transition metal ions located at the center of the octahedron form a kagome lattice sandwiched by two sheets of halogen ions [see Fig. 1a]. In the breathing lattice, transition metal ions are trimerized through forming metal-metal bonds, resulting in alternating arrangements of adjacent large and small triangles [see Fig. 1b]. This structural distortion breaks the spatial inversion symmetry, reducing the symmetry to the polar space group $P3m1$, thus allowing the emergence of out-of-plane polarization. Polarization can be reversed by switching the breathing mode, wherein the trimerization shifts to the adjacent large triangle [see Fig. 1b]. At present, Nb_3X_8 is the only experimentally confirmed material family in this system with breathing mode²⁴. A few other M_3X_8 ($M = Ti, Ta, W$) monolayers have been predicted to exhibit breathing mode, where ferroelectricity induced by

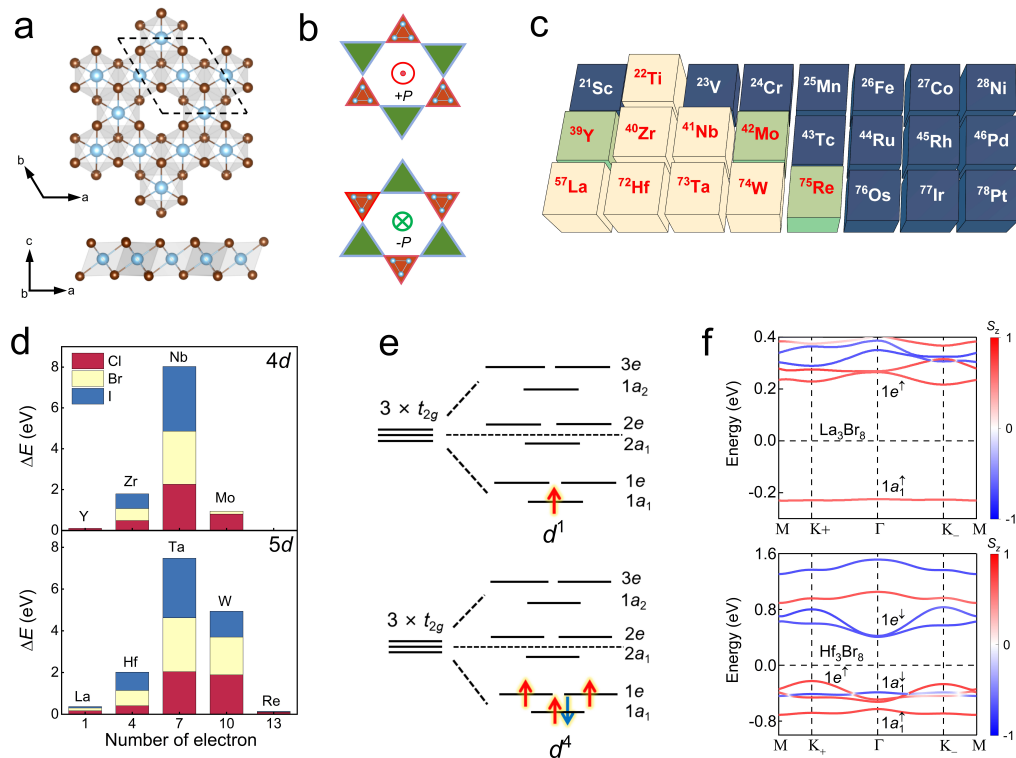


Fig. 1. Screening of M_3X_8 monolayers with breathing mode. **a** Top and side views of the crystal structure of M_3X_8 monolayers. **b** Out-of-plane polarization induced by breathing mode and its sign switching. **c** Screened materials with breathing mode in their ground state structures. Yellow and dark blue fills represent, respectively, the presence and absence of breathing mode in materials containing the corresponding transition metal element. The green fill represents that the breathing mode only occurs in materials containing certain halogen elements. **d** Energy barrier for switching breathing mode. The number on the horizontal axis represents the number of d electrons contained in each M_3 trimer. **e** Schematic illustration of the molecular orbital formed by trimerization and the two configurations of electron occupation. **f** Spin-resolved band structures of La_3Br_8 and Hf_3Br_8 , corresponding to the two occupation configurations in **e**, respectively.

breathing mode was proposed, but generally with very high energy barriers^{26–29}.

We first screened materials with breathing mode throughout the M_3X_8 monolayer system, where M includes all $3d/4d/5d$ transition metal ions. As shown in Fig. 1c, the breathing mode is widely present in materials containing early $4d$ and $5d$ transition metal ions, whereas for the $3d$ series, it only occurs in Ti_3X_8 monolayers. This phenomenon is related to the fact that $4d/5d$ orbitals are more extended and thus more prone to form metal-metal bonding with respect to $3d$ orbitals. All materials with breathing mode in their ground-state structures show dynamic stability except for Re_3I_8 monolayer [see Supplementary Fig. 1].

For the $4d$ and $5d$ series, the energy reduction caused by the breathing mode exhibits a non-monotonic trend with increasing atomic number, reaching the maximum at the middle Nb and Ta, respectively [see Fig. 1d]. This trend is attributed to the change in molecular orbital occupation in an isolated M_3X_{13} cluster, consisting of three edge-sharing octahedra. Figure 1e shows the molecular orbitals formed by the t_{2g} orbitals. The number of elec-

trons occupying the molecular orbitals is $3n-2$, where n represents the order number of M element in the transition metal series of the same period. When the occupancy is less than half full ($3n-2 < 9$), the energy levels of all occupied molecular orbitals are lower than that of the t_{2g} orbitals, resulting in an increase in energy gain from trimerization with the increase in the number of valence electrons. When the occupancy exceeds half full, the energy level of the highest occupied molecular orbital is higher than that of the t_{2g} orbitals. Consequently, the energy gain gradually decreases as the number of valence electrons increases [see Fig. 1d]. This trend further explains why the breathing mode only appears in the early part of the transition metal series.

Depending on the parity of n , the highest occupied states are the up spin states of the single and doubly degenerate orbitals, respectively [see Fig. 1d], resulting in a total magnetic moment of 1 or 2 μ_B for each cluster. All materials with breathing mode exhibit insulating behavior, similar to Nb_3X_8 . The band gap, depending on the specific materials, may be opened by crystal field splitting or Coulomb repulsion interaction, corresponding

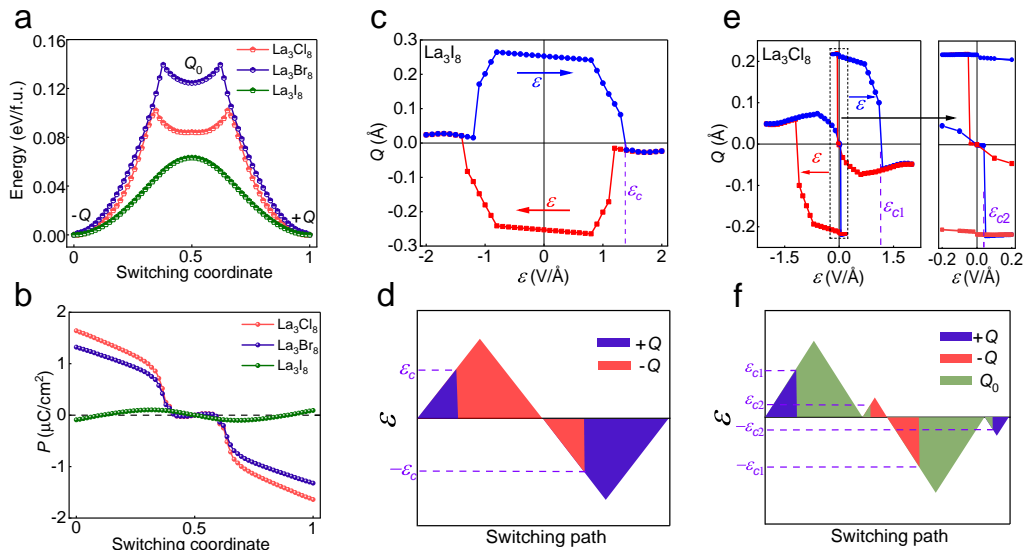


Fig. 2. Ferroelectric switching induced by electric field. Changes in **a** energy and **b** ferroelectric polarization of La_3X_8 monolayers along the switching path. **c,d** Changes in the amplitude and sign of breathing mode in La_3I_8 monolayer induced by pulsed electric field. The blue and red arrows represent the process of increasing and decreasing the electric field, respectively. **e** Electric field-induced change in the breathing mode of La_3Cl_8 monolayer. The right inset shows the switching of the breathing mode induced by a small electric field near the paraelectric phase. **f** The applied pulse electric field and resulting sign switching of breathing mode. Q_0 represents the intermediate state in which the breathing mode disappears upon removal of the electric field.

to the charge-transfer type and Mott insulators, respectively [see Fig. 1f]. In addition, flat bands similar to those of Nb_3X_8 also emerge in other materials, such as La_3Br_8 monolayer, whose highest occupied valence band forms a flat band with a bandwidth of only 6 meV. Therefore, this 2D kagome system provides an ideal platform for studying flat-band related physics and Mott insulators driven by breathing mode.

Control of breathing mode by electric field. For materials with cations in the middle of the series, such as Nb_3X_8 , the high energy barrier prevents their polarization from being reversed by an external electric field. To verify the accessibility of ferroelectric switching, we focus on materials with cations at the beginning of the 5d series, La_3X_8 ($X = \text{Cl}, \text{Br}, \text{I}$) monolayers, which exhibit low energy barriers. Figure 2a shows their energy variation along the ferroelectric switching path. Interestingly, the La_3Cl_8 and La_3Br_8 monolayers exhibit potential well-type energy curves around the paraelectric phase, that is, their energy variation trends change during the transition from ferroelectric to paraelectric phase. This change in trend can be attributed to the emergence of trimerization caused by enhanced breathing mode, which leads to a metal-insulator transition [see Supplementary Fig. 2]. The ferroelectric polarization also exhibits a nonmonotonic variation along the switching path, and undergoes a sign change when transitioning toward the paraelectric phase [see Fig. 2b]. The two polar modes contributing to the polarization are both coupled to the breathing mode,

but they exhibit opposite signs and different trends [see Supplementary Fig. 3], which may be responsible for the complex behavior of ferroelectric polarization.

Then the switching of the breathing mode caused by an out-of-plane electric field is demonstrated. Figure 2c shows the evolution of the breathing mode in La_3I_8 monolayer under one electric field cycle. The amplitude of the breathing mode changes slightly initially and then decreases rapidly as the electric field increases. It undergoes a sign reversal when the electric field reaches a critical value ε_c , and remains roughly constant with further increases in the electric field. When the electric field decreases below the critical value, the breathing mode gradually transitions to the state opposite to its initial one. Then applying an electric field in the opposite direction causes the breathing mode to undergo a similar transition process and eventually return to its initial state. Figure 2d depicts the applied electric field pulse and the corresponding switch in the sign of the breathing mode. Other modes also undergo similar transitions, among which the polar mode of anions at general positions shows a strong positive correlation with the electric field, suggesting it as the primary driving force for electric field-induced structural transformation [see Supplementary Fig. 4].

Interestingly, the breathing mode of La_3Cl_8 monolayer exhibits a more complex behavior under the action of a cyclic electric field [see Fig. 2e]. When the electric field exceeds a critical value, the amplitude of the breathing mode decreases sharply and undergoes a sign change,

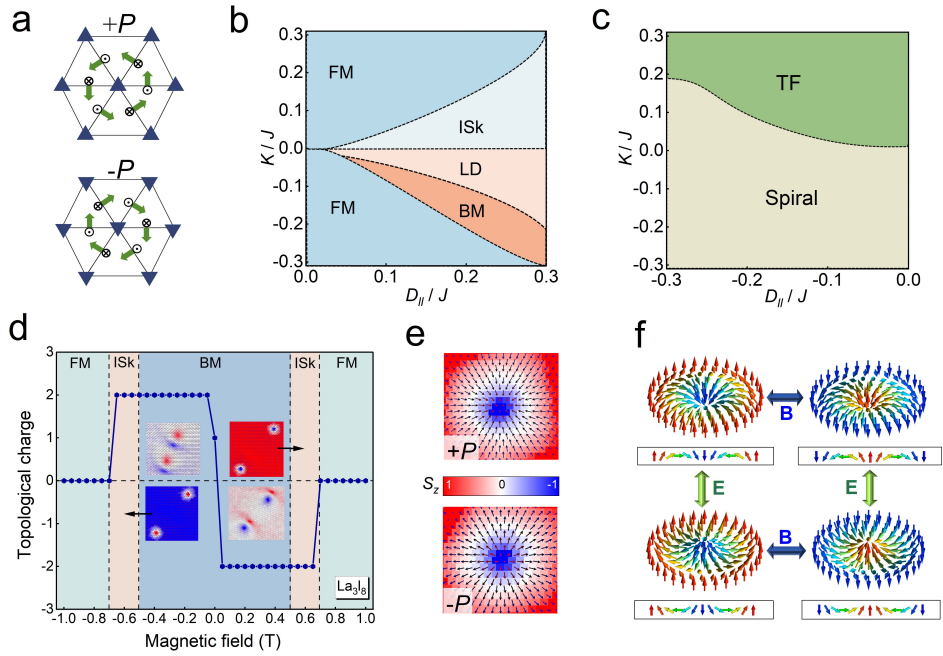


Fig. 3. Transition of topological magnetic structure under external field. **a** DM vectors of the nearest-neighbor bonds in two opposite polarization states. Magnetic phase diagrams under **b** ferromagnetic and **c** antiferromagnetic neighbor exchange interaction. The magnetic phases that emerge include ferromagnetic (FM), isolated skyrmion (ISk), labyrinth domain (LD), and bimeron (BM), triangular antiferromagnetic (TF) and spiral spin phases. **d** Transition of magnetic phase and topological charge of La_3I_8 monolayer with out-of-plane magnetic field. **e** Spin textures of skyrmion appearing in two opposite polarization states. **f** Schematic illustrating the switching of the chirality and topological charge of skyrmions by external electric and magnetic fields, respectively.

similar to the behavior of La_3I_8 monolayer. However, the difference is that as the electric field weakens, the breathing mode gradually disappears instead of transitioning to a state opposite to the initial one. Then when a small positive electric field is applied, the breathing mode changes dramatically to the opposite state from the initial one [see the inset of Fig. 2e]. Applying an electric field in the opposite direction induces a similar transition, returning the breathing mode from the opposite state to its initial state. Therefore, ferroelectric switching is accomplished in two steps, that is, first switching to the paraelectric phase without breathing mode by applying a larger pulse electric field, and then transitioning to the opposite polarization state via a smaller pulse electric field [see Fig. 2f]. This multistep transition is attributed to the metastability of the paraelectric phase [see Fig. 2a]. These results demonstrate that in this system, not only the sign of the breathing mode but also its emergence can be controlled by the electric field.

Switching of topological magnetic structure. The breathing mode causes each trimer to carry a magnetic moment, transforming the breathing kagome lattice into a triangular magnetic lattice. In addition, inversion symmetry breaking may give rise to topological magnetic textures induced by Dzyaloshinskii-Moriya (DM) interactions^{37–41}. Symmetry analysis reveals that switch-

ing the breathing mode reverses the DM vectors of adjacent trimers [see Fig. 3a]. Figure 3b shows the evolution of the magnetic phase as a function of the DM interaction and the magnetic anisotropy under a ferromagnetic neighbor exchange interaction. With increasing DM interaction, the ferromagnetic phase transforms into an isolated skyrmion or a bimeron phase, depending on the easy-axis or easy-plane anisotropy, respectively [see Fig. 3b], which is consistent with previous observations^{42, 43}. The critical value of DM interaction for phase transition increases with the anisotropy constant. A topological trivial texture, the labyrinth domain, emerges between these two topological phases. As for the antiferromagnetic exchange interaction, easy-axis anisotropy leads to a spiral spin order, while easy-plane anisotropy energetically prefers the triangular antiferromagnetic structure [see Fig. 3c].

Then the magnetic ground states of all materials with breathing modes were determined by Monte Carlo simulations based on the calculated magnetic parameters [see Supplementary Figs. 5, 6 and Table 1]. This system exhibits a rich variety of magnetic phases, involving ferromagnetic, triangular antiferromagnetic, spiral spin, and bimeron phases. The skyrmion phase is absent because almost all materials exhibit easy-plane anisotropy. The emergence of ferromagnetism in some materials such

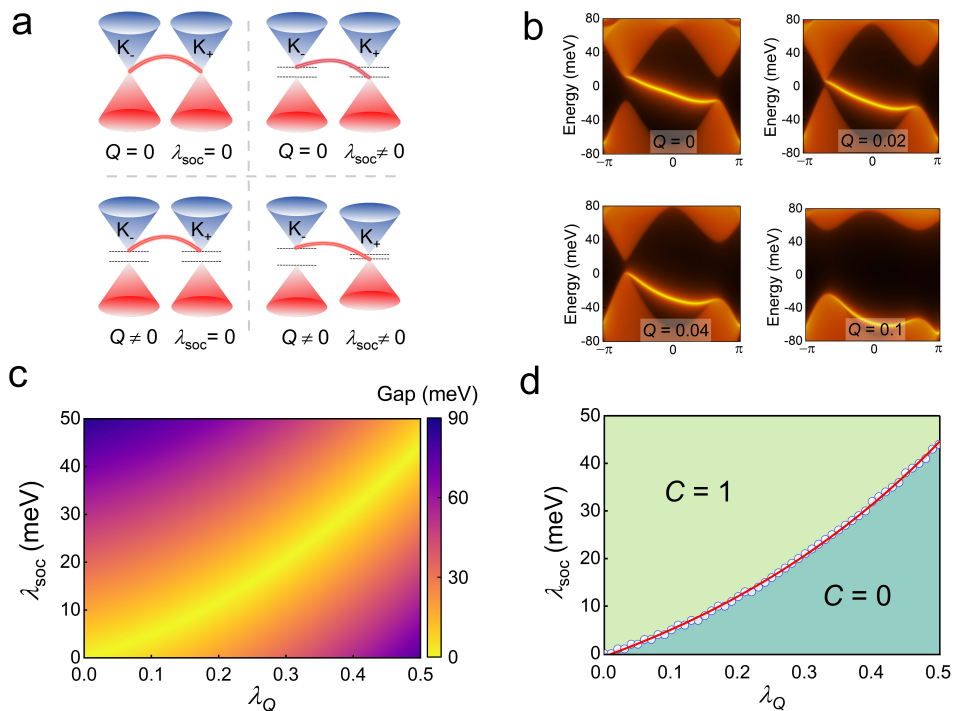


Fig. 4. Topological phase transition induced by change in breathing mode. **a** Schematic of the splitting of the Dirac band and the resulting surface states in the presence or absence of breathing mode and SOC. **b** Transformation of surface states induced by enhanced breathing mode in La_3Cl_8 monolayer embedded with K ions. **c** Variation of the band gap with the amplitude of the breathing mode and the SOC constant. The strength of the breathing mode is represented by the relative difference between the nearest-neighbor (t_1) and next-nearest-neighbor (t_2) transition integrals ($\lambda_Q = 1 - t_2/t_1$). **d** Chern number as a function of the amplitude of the breathing mode and the SOC constant.

as La_3X_8 ($X = \text{Cl}, \text{Br}$) monolayers suggests that this system provides a versatile platform for realizing 2D multiferroics^{44–46}.

Next, the La_3I_8 monolayer, exhibiting a topological bimeron phase, is taken as a representative example to demonstrate the modulation effect of an external field. A small out-of-plane magnetic field drives the bimeron phase into the isolated skyrmion phase, which subsequently transforms into the ferromagnetic phase as the magnetic field is further increased [see Fig. 3d]. Applying a magnetic field in the opposite direction induces similar magnetic phase transitions, but with the opposite sign of the topological charge. Similar magnetic phase transitions also occur in other materials [see Supplementary Fig. 7]. Moreover, in the opposite polarization state, the chirality of the skyrmion is changed due to the reversal of the DM vectors [see Fig. 3e]. Therefore, in this system, the chirality and topological charge of the topological magnetic texture can be controlled by the electric and magnetic fields, respectively, as depicted in Fig. 3f.

Topological phase transition driven by breathing mode. In an ideal kagome lattice, the inclusion of spin-orbit coupling (SOC) opens a gap at the Dirac point (K point), resulting in a non-trivial topological insulating state with robust gapless edge states⁶ [see Fig. 4a].

The breathing modes also opens a band gap at the Dirac point, however, unlike SOC, the induced insulating state is topologically trivial. Despite the broken inversion symmetry, the band gaps at K_+ and K_- valleys, opened by the breathing mode, are equal due to the protection of vertical mirror symmetry. Including both SOC and breathing mode breaks the valley degeneracy while preserving the non-trivial topological insulating state [see Fig. 4a]. Note that the Fermi level usually does not lie within the band gap at the Dirac points due to the $1/3$ filling of the highest occupied d orbital, resulting in a metallic state for the prototype phase. To obtain a realistic topological insulator, the Fermi level of the prototype phase can be raised into the band gap at the Dirac point by inserting alkali metal ions [see Supplementary Fig. 8 and Table 2]. The optimal site for alkali metal ion absorption is the center of the hexagon, where the magnetic ground state remains unchanged.

The band gaps at the Dirac points are significantly affected by the amplitude of the breathing mode. In the absence of SOC, the band gaps at both valleys increase as the breathing mode is enhanced. In contrast, in the presence of SOC, the two band gaps exhibit opposite trends, with one of them closing first and then reopening, signaling a topological phase transition [see Supplementary

Fig. 9]. The topological phase transition caused by the change in the breathing mode is confirmed by the transition of the edge state [see Fig. 4b]. The tight-binding model calculations show that the critical amplitude of the breathing mode required to close the band gap is linearly proportional to the SOC intensity [see Fig. 4c and Supplementary Fig. 10]. Increasing or decreasing the mode amplitude near the critical value drives the system into topologically trivial and non-trivial insulating phases, respectively [see Fig. 4d]. These results indicate that the emergence of topological insulating phase is determined by the competition between SOC and breathing mode, and the critical values of both vary as exponential function of $\lambda_{SOC}^c \propto e^{\alpha\lambda_Q^c} - 1$. Therefore, modulation of the breathing mode by electric field enables topological phase transitions, such as the transition from a topologically trivial insulator to a Chern insulator, driven by the ferroelectric-to-paraelectric phase transition in the La_3Cl_8 monolayer.

In conclusion, the M_3X_8 monolayer system provides a broad platform for studying topological quantum states, topological spin textures and multiferroics related to the breathing mode. The breathing mode mainly occurs in materials containing early $4d/5d$ transition metal ions, and materials at both ends of the series exhibit low energy barriers for ferroelectric switching. The breathing mode is coupled with the polar mode and can be switched in sign or even eliminated by an external electric field. Importantly, the coupling of the breathing mode with magnetic parameters and band topology provides a key degree of freedom for realizing electric-field control of topological spin textures and electronic states. Our discovery presents a paradigm system for studying exotic quantum phenomena associated with the breathing mode in kagome lattice and can inspire the exploration of electric-field control of topological quantum states.

Methods

First-principles calculations. The first-principles calculations based on density functional theory (DFT) were performed using the projector-augmented-wave (PAW)⁴⁷ method, as implemented in the Vienna *ab initio* simulation package (VASP)⁴⁸. The Perdew-Burke-Ernzerhof functional was used as the exchange-correlation functional. The Hubbard U method within the rotationally invariant formalism was used to treat the electron correlation in the d shell of transition-metal ions⁴⁹, and the effective U values [Supplementary see Table 3] were determined by self-consistent calculation based on the constrained random-phase approximate method⁵⁰. For each monolayer, a vacuum space of 20 Å was used to separate the neighboring images along the vertical direction. A plane-wave cutoff energy of 500 eV was used for the plane-wave expansion and a convergence threshold of 10^{-8} eV was used for the electronic self-consistency

loop. A Γ -centered $7 \times 7 \times 1$ k -point mesh was used for the Brillouin-zone integration. The in-plane (IP) lattice constants and internal atomic coordinates were relaxed until the Hellman-Feynman force on each atom was less than 10^{-3} eV/Å. The ISOTROPY tool⁵¹ was used to determine the amplitudes of the structural distortion modes. The energy barriers of ferroelectric switching were calculated using the climbing nudged elastic band method⁵². The Born effective charge was calculated by density functional perturbation theory (DFPT), and is used to calculate the ferroelectric polarization. The phonon frequencies and corresponding eigenmodes were calculated on the basis of the extracted force-constant matrices, as implemented in the PHONOPY code⁵³. The maximally localized Wannier functions were constructed using the WANNIER90 package⁵⁴, and the WannierTools code⁵⁵ was used to calculate the edge states.

Monte Carlo simulations. Monte Carlo simulations were performed to determine the magnetic ground states of materials and study the magnetic phase diagram that varies with magnetic parameters and external magnetic field. The following spin Hamiltonian

$$H = - \sum_{i,j} J_{ij} \mathbf{S}_i \cdot \mathbf{S}_j - \sum_{i,j} \mathbf{D}_{ij} \cdot (\mathbf{S}_i \times \mathbf{S}_j) - \sum_i K (S_i^z)^2 - \mu_M B \sum_i S_i^z$$

was adopted, where J_{ij} contains all the magnetic exchange parameters considered, \mathbf{D}_{ij} is the DM vector, K is the single-ion magnetic anisotropy constant, μ_M and B represents the spin moment of each trimer and the external magnetic field, respectively. A 128×128 spin lattice with periodic boundary conditions and the annealing algorithm were used in the simulations. For each temperature, 10^6 steps were taken to reach equilibrium and 10^6 steps were performed for sampling by using the Metropolis algorithm.

Tight-binding model. The tight-binding model on a breathing kagome lattice was constructed to study the topological phase diagram that varies with the breathing mode and SOC constant. The Hamiltonian can be expressed as

$$H = \sum_{\langle i,j \rangle} t_1 c_i^\dagger c_j + i\lambda_{soc} \sum_{\langle i,j \rangle} v_{ij} c_i^\dagger s_z c_j + M \sum_i c_i^\dagger s_z c_i + \sum_i \epsilon_i c_i^\dagger c_i + H.c.,$$

where the hopping parameters are up to the third-nearest neighbors. The second and third terms represent the intrinsic SOC and the magnetic exchange terms, respectively, while the fourth term introduces an on-site potential energy.

Data availability

The authors declare that the data supporting the findings of this study are available within the article and the

corresponding Supporting Information file. All other relevant source data are available from the corresponding author upon reasonable request.

Code availability

Tight-binding model and Monte Carlo simulations codes are available from the corresponding author upon reasonable request.

References

-
- * juntingzhang@cumt.edu.cn
- Ortiz, B. R. *et al.* CsV₃Sb₅ : A Z₂ Topological Kagome Metal with a Superconducting Ground State. *Phys. Rev. Lett.* **125**, 247002 (2020).
 - Liang, Z. *et al.* Three-Dimensional Charge Density Wave and Surface-Dependent Vortex-Core States in a Kagome Superconductor CsV₃Sb₅. *Phys. Rev. X* **11**, 031026 (2021).
 - Zhou, Y., Kanoda, K. & Ng, T.-K. Quantum spin liquid states. *Rev. Mod. Phys.* **89**, 025003 (2017).
 - Kang, M. *et al.* Dirac fermions and flat bands in the ideal kagome metal fesn. *Nat. Mater.* **19**, 163–169 (2019).
 - Yin, J.-X. *et al.* Discovery of charge order and corresponding edge state in kagome magnet fege. *Phys. Rev. Lett.* **129**, 166401 (2022).
 - Wang, Y., Wu, H., McCandless, G. T., Chan, J. Y. & Ali, M. N. Quantum states and intertwining phases in kagome materials. *Nature Reviews Physics* **5**, 635–658 (2023).
 - Ortiz, B. R. *et al.* Superconductivity in the Z₂ kagome metal KV₃Sb₅. *Phys. Rev. Materials* **5**, 034801 (2021).
 - Mielke, C. *et al.* Time-reversal symmetry-breaking charge order in a kagome superconductor. *Nature* **602**, 245–250 (2022).
 - Nie, L. *et al.* Charge-density-wave-driven electronic nematicity in a kagome superconductor. *Nature* **604**, 59–64 (2022).
 - Chen, H. *et al.* Roton pair density wave in a strong-coupling kagome superconductor. *Nature* **599**, 222–228 (2021).
 - Li, H. *et al.* Observation of Unconventional Charge Density Wave without Acoustic Phonon Anomaly in Kagome Superconductors AV₃Sb₅ (X = Rb , Cs). *Phys. Rev. X* **11**, 031050 (2021).
 - Xu, Y. *et al.* Three-state nematicity and magneto-optical kerr effect in the charge density waves in kagome superconductors. *Nat. Phys.* **18**, 1470–1475 (2022).
 - Kang, M. *et al.* Twofold van Hove singularity and origin of charge order in topological kagome superconductor CsV₃Sb₅. *Nat. Phys.* **18**, 301–308 (2022).
 - Yang, S.-Y. *et al.* Giant, unconventional anomalous Hall effect in the metallic frustrated magnet candidate, KV₃Sb₅. *Sci. Adv.* **6** (2020).
 - Xu, G., Lian, B. & Zhang, S.-C. Intrinsic Quantum Anomalous Hall Effect in the Kagome Lattice Cs₂LiMn₃F₁₂. *Phys. Rev. Lett.* **115**, 186802 (2015).
 - Ye, L. *et al.* Massive dirac fermions in a ferromagnetic kagome metal. *Nature* **555**, 638–642 (2018).
 - Tang, E., Mei, J.-W. & Wen, X.-G. High-temperature fractional quantum hall states. *Phys. Rev. Lett.* **106**, 236802 (2011).
 - Liu, H. *et al.* High-temperature fractional quantum hall state in the floquet kagome flat band. *Phys. Rev. B* **105**, 1161108 (2022).
 - Hou, Z. *et al.* Observation of various and spontaneous magnetic skyrmionic bubbles at room temperature in a frustrated kagome magnet with uniaxial magnetic anisotropy. *Adv. Mater.* **30** (2018).
 - Li, Z. *et al.* Electron-Assisted Generation and Straight Movement of Skyrmion Bubble in Kagome TbMn₆Sn₆. *Adv. Mater.* **36** (2024).
 - Hirschberger, M. *et al.* Skyrmion phase and competing magnetic orders on a breathing kagomé lattice. *Nat. Commun.* **10** (2019).
 - Ezawa, M. Higher-order topological insulators and semimetals on the breathing kagome and pyrochlore lattices. *Phys. Rev. Lett.* **120**, 026801 (2018).
 - Bolens, A. & Nagaosa, N. Topological states on the breathing kagome lattice. *Phys. Rev. B* **99**, 165141 (2019).
 - Pasco, C. M., El Baggari, I., Bianco, E., Kourkoutis, L. F. & McQueen, T. M. Tunable Magnetic Transition to a Singlet Ground State in a 2D van der Waals Layered Trimerized Kagomé Magnet. *ACS Nano* **13**, 9457–9463 (2019).
 - Peng, R. *et al.* Intrinsic anomalous valley Hall effect in single-layer Nb₃I₈. *Phys. Rev. B* **102**, 035412 (2020).
 - Li, Y., Liu, C., Zhao, G.-D., Hu, T. & Ren, W. Two-dimensional multiferroics in a breathing kagome lattice. *Phys. Rev. B* **104**, 1060405 (2021).
 - Zhao, J., Feng, Y., Dai, Y., Huang, B. & Ma, Y. Ferroelectrovalley in two-dimensional multiferroic lattices. *Nano Lett.* **24**, 10490–10495 (2024).
 - Hu, D. *et al.* Two-dimensional 5d multiferroic W₃Cl₈ : Breathing kagome lattice and tunable magneto-optical Kerr effect. *Phys. Rev. B* **109**, 014433 (2024).
 - Xing, S., Wang, B., Zhao, T., Zhou, J. & Sun, Z. Independent Electrical Control of Spin and Valley Degrees in 2D Breathing Kagome Ta₃I₈ with Intrinsic Triferroicity. *The Journal of Physical Chemistry Letters* **15**, 6489–6495 (2024).
 - Sun, Z. *et al.* Observation of Topological Flat Bands in the Kagome Semiconductor Nb₃Cl₈. *Nano Lett.* **22**, 4596–4602 (2022).
 - Regmi, S. *et al.* Spectroscopic evidence of flat bands in breathing kagome semiconductor Nb₃I₈. *Communications Materials* **3** (2022).
 - Zhang, H. *et al.* Topological Flat Bands in 2D Breathing-Kagome Lattice Nb₃TeCl₇. *Adv. Mater.* **35** (2023).
 - Gao, S. *et al.* Discovery of a single-band mott insulator in a van der waals flat-band compound. *Phys. Rev. X* **13**, 041049 (2023).
 - Grytsiuk, S., Katsnelson, M. I., Loon, E. G. v. & Rösner, M. Nb₃Cl₈: a prototypical layered Mott-Hubbard insulator. *npj Quantum Materials* **9** (2024).
 - Schaffer, R., Huh, Y., Hwang, K. & Kim, Y. B. Quantum spin liquid in a breathing kagome lattice. *Phys. Rev. B* **95**, 054410 (2017).
 - Hu, J. *et al.* Correlated flat bands and quantum spin liquid state in a cluster mott insulator. *Communications Physics* **6** (2023).

37. Seki, S., Yu, X. Z., Ishiwata, S. & Tokura, Y. Observation of skyrmions in a multiferroic material. *Science* **336**, 198–201 (2012).
38. Kézsmárki, I. *et al.* Néel-type skyrmion lattice with confined orientation in the polar magnetic semiconductor GaV₄S₈. *Nat. Mater.* **14**, 1116–1122 (2015).
39. Fert, A., Reyren, N. & Cros, V. Magnetic skyrmions: advances in physics and potential applications. *Nat. Rev. Mater.* **2** (2017).
40. Xu, C. *et al.* Electric-field switching of magnetic topological charge in type-i multiferroics. *Phys. Rev. Lett.* **125**, 037203 (2020).
41. Yu, D., Ga, Y., Liang, J., Jia, C. & Yang, H. Voltage-controlled dzyaloshinskii-moriya interaction torque switching of perpendicular magnetization. *Phys. Rev. Lett.* **130**, 056701 (2023).
42. Göbel, B., Mook, A., Henk, J., Mertig, I. & Tretiakov, O. A. Magnetic bimerons as skyrmion analogues in in-plane magnets. *Phys. Rev. B* **99**, 060407 (2019).
43. Göbel, B., Mertig, I. & Tretiakov, O. A. Beyond skyrmions: Review and perspectives of alternative magnetic quasiparticles. *Phys. Rep.* **895**, 1–28 (2021).
44. Zhang, J. *et al.* Design of two-dimensional multiferroics with direct polarization-magnetization coupling. *Phys. Rev. Lett.* **125**, 017601 (2020).
45. Zhang, J. *et al.* Coexistence and coupling of spin-induced ferroelectricity and ferromagnetism in perovskites. *Phys. Rev. Lett.* **129**, 117603 (2022).
46. Wang, F., Zhou, Y., Shen, X., Dong, S. & Zhang, J. Magnetoelectric coupling and cross control in two-dimensional ferromagnets. *Phys. Rev. Applied* **20**, 064011 (2023).
47. Blöchl, P. E. Projector augmented-wave method. *Phys. Rev. B* **50**, 17953–17979 (1994).
48. Kresse, G. & Furthmüller, J. Efficiency of ab-initio total energy calculations for metals and semiconductors using a plane-wave basis set. *Nato. Sc. S. Ss. Iii. C. S.* **6**, 15–50 (1996).
49. Dudarev, S. L., Botton, G. A., Savrasov, S. Y., Humphreys, C. J. & Sutton, A. P. Electron-energy-loss spectra and the structural stability of nickel oxide: An LSDA+U study. *Phys. Rev. B* **57**, 1505 (1998).
50. Şaşoğlu, E., Friedrich, C. & Blügel, S. Effective coulomb interaction in transition metals from constrained random-phase approximation. *Phys. Rev. B* **83**, 121101 (2011).
51. Campbell, B. J., Stokes, H. T., Tanner, D. E. & Hatch, D. M. *ISODISPLACE*: a web-based tool for exploring structural distortions. *J. Appl. Crystallogr.* **39**, 607 (2006).
52. Sheppard, D., Xiao, P., Chemelewski, W., Johnson, D. D. & Henkelman, G. A generalized solid-state nudged elastic band method. *J. Chem. Phys.* **136** (2012).
53. Togo, A. & Tanaka, I. First principles phonon calculations in materials science. *Scripta Mater.* **108**, 1–5 (2015).
54. Pizzi, G. *et al.* Wannier90 as a community code: new features and applications. *J. Phys. Condens. Matter* **32**, 165902 (2020).
55. Wu, Q., Zhang, S., Song, H.-F., Troyer, M. & Soluyanov, A. A. Wanniertools: An open-source software package for novel topological materials. *Comput. Phys. Commun.* **224**, 405–416 (2018).

Acknowledgements

This work was financially supported by the National Natural Science Foundation of China (Grants No. 12374097 and No. 11974418), and the Postgraduate Research & Practice Innovation Program of Jiangsu Province (grant number KYCX24_2693). Computer resources provided by the High Performance Computing Center of Nanjing University are gratefully acknowledged.

Author contributions

J. T. Zhang conceived the idea and wrote the manuscript. Y. Xie performed the first-principles calculation, Monte Carlo simulation, and tight-binding model analysis. K. Ji and J. He analyzed the results and discussed with Y. Xie. Y. Xie and X. F. Shen prepared the figures. D. H. Wang discussed the results of the tight-binding model and revised the manuscript. All authors discussed the results and commented on the manuscript.

Additional information

Supplementary information is available for this paper.

Correspondence and requests for materials should be addressed to J. T. Zhang.